



Conditional flow field statistics of jet-in-hot-coflow flames



Ernst Oldenhof, Mark J. Tummers*, Eric H. van Veen, Dirk J.E.M. Roekaerts

Department of Process and Energy, section Fluid Mechanics, Delft University of Technology, Mekelweg 2, 2628 CB Delft, The Netherlands

ARTICLE INFO

Article history:

Received 13 May 2012

Received in revised form 3 March 2013

Accepted 4 March 2013

Available online 18 April 2013

Keywords:

Conditional statistics

Simultaneous PIV/OH-PLIF

Jet-in-hot-coflow

Flameless combustion

ABSTRACT

The conditional velocity field of the Delft jet-in-hot-coflow flames is studied by the simultaneous application of planar laser-induced fluorescence of the OH radical (OH-PLIF) and particle image velocimetry (PIV). The goal of this study is to assess the role of turbulence on chemical processes in the Delft jet-in-hot-coflow flames and similar setups, that are characterised by the presence of a turbulent jet that issues into a slower-moving and much less turbulent surroundings of combustion products. An important result is that the conditional velocity field (conditional on the presence of a strong OH signal) is very different from the non-conditional velocity field at the same location. These jet-in-hot coflow flames are thus characterised by a strong intermittency, and experience a very different flow field and flow time scales than one would expect from the local mean velocity and scalar field. An other result following from the local velocity data is that the average conditional strain perpendicular to the flame surface is neither compressive nor extensive. This is caused by the orientation of the principle strains and that of the flame interface. One millimetre inward to the jet, from the edge of the fuel-rich side of the OH contours, the average strains do become compressive, and the pdf of normal strain becomes considerably wider. In light of these results, the closure of the mean chemical source term by introducing a single (unconditional) turbulent time scale seems to be an invalid approach. Furthermore, it demonstrates that the fluid dynamic properties of the coflow stream are decisive for the applicability of these setups to the study of turbulence-chemistry interaction in industrial combustion processes.

© 2013 The Combustion Institute. Published by Elsevier Inc. All rights reserved.

1. Introduction

Flames created by the injection of a gaseous fuel in hot, low-oxygen surroundings have received considerable attention in the past decade. This is due to the relevance of these flames to novel, clean combustion techniques in which a strong recirculation of flue gases and heat regeneration are employed. An issue that has been addressed frequently is how such flames are stabilised, and how this stabilisation can be dealt with numerically. Studies on several different laboratory setups have made apparent that knowledge of autoignition processes is key to understanding the flame stabilisation for these type of flames [1–5]. Furthermore, theoretical, experimental and numerical studies have shown that the flow field can seriously impact the autoignition process, by steepening scalar gradients and thereby augmenting transport of species and heat away from a potential ignition spot [6–8]. An other aspect that makes the flow field especially relevant to these flames is their lower adiabatic flame temperature, which increases the chemical time scales to a point where they are of the same order of magnitude as the flow time scales, an often cited cause for the “volumetric” nature of the combustion zone, and the flat temperature field [9,10].

The experimental studies intended to probe the nature of the flame stabilisation have often elaborated the chemical aspects, by providing datasets of concentrations of chemical species [2,11] or by planar imaging of selected species relevant to autoignition [12,13]. The flow field has perhaps been somewhat underexposed, and where available, velocity information has been limited to one-point, non-conditional statistics [14,15].

In the following, detailed conditional velocity statistics will be discussed, that were obtained by the simultaneous application of Particle Image Velocimetry (PIV) and Planar Laser Induced Fluorescence measurements of the OH radical (OH-PLIF). This is an established combination of techniques applied to both premixed [16] and unpremixed [17] flames, and it has recently been extended to high repetition-rate measurements [18,19]. Nevertheless, to the author's knowledge, it has not yet been applied to hot-coflow flames.

The aim of this article is to provide new insights into the local flame structure of laboratory-scale jet-in-hot-coflow flames. This insight can help in judging the applicability of the different combustion models that are available, and in understanding the nature of the turbulence-chemistry interaction in these flames. Additionally, the suitability of these setups to the study of industrial sized burners will be discussed.

* Corresponding author. Fax: +31 15 27 82838.

E-mail address: M.J.Tummers@tudelft.nl (M.J. Tummers).

2. Experimental setup

2.1. DJHC burner

In this paper, flames are studied that were generated with the Delft jet-in-hot-coflow (DJHC) burner. The most characteristic element of this setup is the secondary burner, enclosed by a steel outer tube, that generates a hot, oxygen deficient coflow stream into which a fuel jet is injected centrally. Figure 1 shows the geometry of the setup, along with the window where measurements were taken (except for the measurements reported in Section 3.2, where the observation window is moved up by 10 mm), corresponding to the region in space where reactions start to emerge. A (z, r) -coordinate system is used with its origin at the centre of the fuel pipe exit, the z -direction pointing upward. This is referred to as the “global” coordinate system.

2.2. Case description

2.2.1. Coflow

The coflow properties (temperature, velocity and oxygen mass fraction) were kept constant in the cases studied. The characteristics of the coflow correspond to the DJHC-I case which is addressed in more detail in [15]. The profiles of axial velocity, mean temperature and oxygen mass fraction are shown in Fig. 2. The average composition of the coflow (mass-averaged between $r = 2.5$ mm and $r = 35$ mm, see also [4]) is, in mass fractions, $Y_{O_2;co} = 7.6\%$, $Y_{CO_2;co} = 10.1\%$, $Y_{H_2O;co} = 8.0\%$ and $Y_{N_2;co} = 74.2\%$.

The Taylor length scale of the coflow has been determined previously with LDA to be around 10 mm. The Taylor-scale Reynolds number Re_λ of the coflow in its centre region at $z = 3$ mm is close to unity (based on the rms of the axial velocity fluctuations, ~ 0.10 m/s, a kinematic viscosity of approximately 200×10^{-6} m²/s and a Taylor length scale in the order of 10 mm). The coflow stream can therefore not be classified as truly turbulent. For instance, in grid turbulence the normalised dissipation rate of turbulent kinetic energy achieves a steady value above $Re_\lambda = 50$ but has an inverse relationship with Re_λ for $Re_\lambda < 10$ [20].

2.2.2. Fuel jet

Three different fuel jets have been considered, with a variation in fuel composition (achieved by premixing of the fuel with air) and in nozzle diameter (2.0 mm inner diameter instead of 4.5 mm). An overview is given in Table 1. Case DNG 4.5 corresponds to the DJHC-I, $Re_{jet} = 8800$ case, as studied earlier [15]. The reported jet Reynolds numbers for the premix 4.5 and the DNG 2.0 cases were determined with the temperature of the fuel jet estimated at 360 K and 470 K, based on earlier determined temperatures with similar jet mass flow rates. The premixing of the fuel (case premix 4.5) was done to study the effect of the stoichiometric mixture fraction, which is roughly six times higher than that of Dutch natural gas (DNG), with the previously given composition of the coflow as oxidiser. The molar composition of DNG is 81.3% methane, 14.4% nitrogen, and some 4% of higher alkanes. The molar composition of the premixed fuel, 3 volumetric parts air on 1 volumetric part DNG (equivalence ratio for combustion in air of 2.82), is 20.4% methane, 63.0% nitrogen, 15.8% oxygen and 0.9% of higher alkanes. The last two columns in Table 1 describe the centreline velocity and the radius of the jet at $z = 70$ mm. The method to determine the jet radius is described in Section 4.2.

The cases do not represent an extensive parametric study, but offer considerable parameter variation. The axial distance of the centre of the measurement plane normalised by the nozzle diameter varies from 16 to 35, and the stoichiometric mixture fraction differs by a factor of 6. The variation in jet Reynolds number is more moderate, varying by a factor of 1.5.

To investigate how premixing affects the ignition process, calculations were done with the SENKIN program [21] (as a constant pressure reactor) using the GRI-MECH 3.0 mechanism [22]. The details of these calculations are discussed in the appendix. The calculations show that the autoignition times of both fuels are similar, but the premixed fuel autoignites earlier at somewhat richer mixture fractions than pure DNG. For both fuels, autoignition seems to take place earliest at relatively lean, sub-stoichiometric mixture fractions.

The length scales in the jet have been discussed in [15]. Summarising, at $(z, r) = (60, 0)$ mm, and with a jet Reynolds number of 8800 and the 4.5 mm nozzle, the longitudinal Taylor length scale is 1.4 mm, and the Taylor-scale Reynolds number is around 90. The Kolmogorov length scale is estimated at 0.10 mm.

2.3. PIV system and data processing

The coflow and the jet stream were both seeded with Al_2O_3 particles, with a nominal diameter of 1 μ m. The particles were illuminated by a laser light sheet that was produced by a Nd:YLF laser (Quantronix Darwin Duo 80-M). The optical setup that combines the PIV and OH-PLIF systems is outlined in Fig. 3. The PIV laser sheet was approximately 40 mm high and 0.8 mm thick. Images were generally taken at 100 Hz, which is the lowest operational repetition rate of the Nd:YLF laser. A 200 mm Nikkor ED lens was used to collect scattered light, the imaged size of one pixel corresponds to 43 μ m. At a 32×32 pixel interrogation window with 50% overlap, this resulted in a vector spacing of 0.69 mm. This suffices to resolve the longitudinal and transversal Taylor length scales (which are between 1 mm and 2 mm at $z = 60$ mm for the Reynolds numbers considered) but not for the Kolmogorov length scale on the jet centreline, which is estimated at 0.1 mm [15]. As stated by Lavoie et al. [23], a resolution of five Kolmogorov length scales or better is required for obtaining velocity derivative estimates (such as the enstrophy, which is reported here) with reasonable accuracy. This is not quite achieved, the enstrophy can therefore be expected to be underestimated in the core-jet region. In the coflow where the length scales are much longer, the deriva-

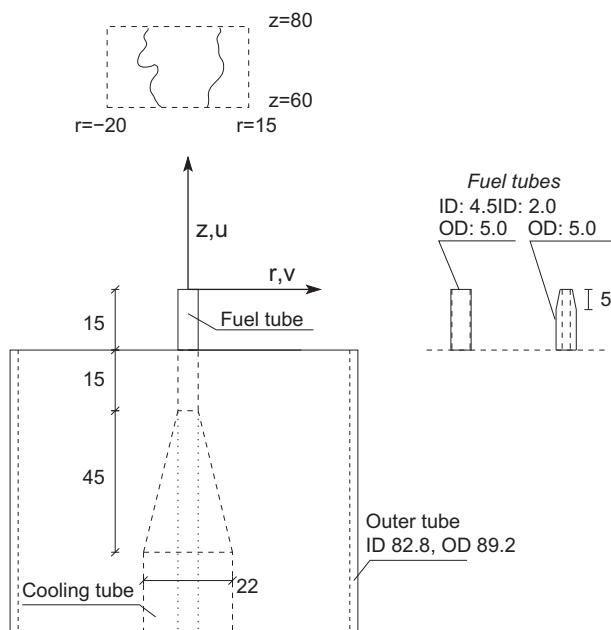


Fig. 1. The geometry of the upper part of the DJHC burner. Dimensions are given in mm. The field of view is indicated with the dashed box. The geometries of the two fuel tubes that were used are shown at the right.

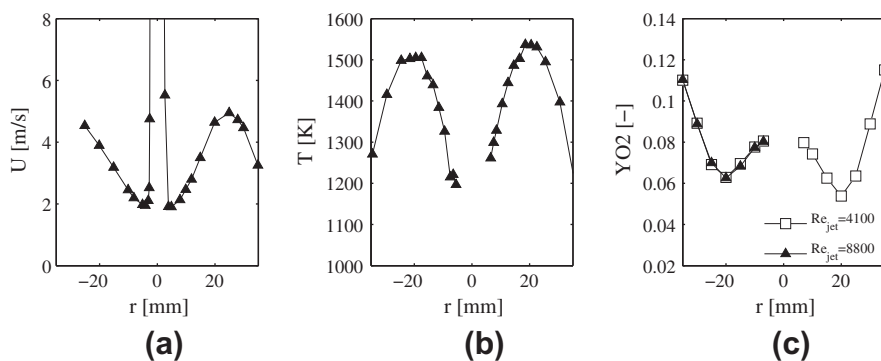


Fig. 2. The coflow characteristics at $z = 3$ mm, of the DJHC-I case with $Re_{jet} = 8800$ and the standard 4.5 mm fuel pipe. Shown are the mean axial velocity as determined with Laser Doppler Anemometry (LDA) (a), the mean temperature, as determined with Coherent anti-Stokes Raman spectroscopy (CARS) (b) and the mean oxygen mass fraction, determined with a flue gas analyser (c). In Fig. 2c, the results for $Re_{jet} = 4100$ were also included.

Table 1
Overview of the test cases for the conditional and local velocity statistics. The fuel ratio given in the second column is volumetric. The stoichiometric mixture fraction ζ_{st} is based on the injected fuel and the coflow properties given in Section 2.2. The maximum equilibrium flame temperature of the premixed fuel is 2023 K, somewhat higher than the 1950 K for the DNG flame.

Case name	Fuel	Nozzle D (mm)	Vol. flow (nl/min)	Re_{jet} (-)	ζ_{st} (-)	$U_{jet,70}$ (m/s)	$r_{jet,70}$ (mm)
DNG 4.5	DNG	4.5	30	8800	0.023	28.2	11.1
premix 4.5	air + DNG (3:1)	4.5	32	9000	0.144	35.6	10.2
DNG 2.0	DNG	2.0	11	5900	0.023	27.9	11.1

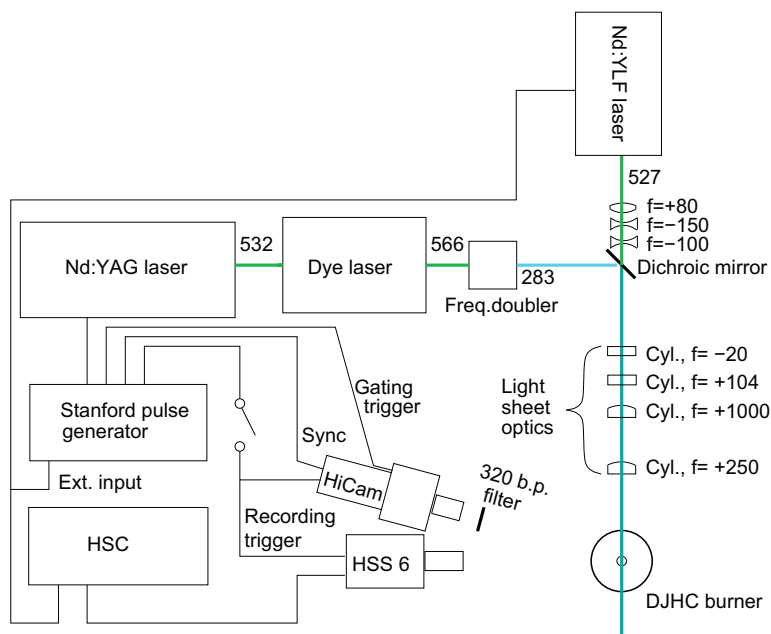


Fig. 3. Schematic overview of the optical setup for the combined PIV and OH-PLIF measurements.

tives are fully resolved. The time interval between the two laser pulses was $30 \mu\text{s}$ at a jet Reynolds number of 4100, $20 \mu\text{s}$ for the DNG 4.5 case and $18 \mu\text{s}$ for the other two cases.

Davis 7.4 was used for the image acquisition and the post-processing. Processing of the raw images was done with multiple cross-correlation passes (three times at a 64×64 window, two times at the final 32×32 window). A reference velocity field of $+6$ m/s was given to aid in the post-processing. A median filter was applied to detect and replace outliers. The rms of the error in axial velocity in the coflow is roughly 0.35 m/s at a shot interval of $30 \mu\text{s}$ and 0.5 m/s at a shot interval of $18 \mu\text{s}$ (based on the known rms values from LDA measurements, which are much lower). These values correspond to 0.1 and 0.15 pixel displacements, a reasonable value for PIV measurements ([24], p. 164–176). The

strains and vorticity were calculated with a central differencing scheme. For the vorticity and normal strains, the error level is estimated at around 350 1/s and 500 1/s for the longer and shorter interval, respectively. For the velocities in the local coordinate system (Section 4), no smoothing was applied. Smoothing with a 3×3 kernel was however applied for the conditional flow properties (Section 3), to reduce variances and statistical error in the coflow region, because of the smaller size of the conditional data. The PIV measurements that were used to determine correlation functions in the coflow were done at 500 Hz repetition rate with a $200 \mu\text{s}$ exposure interval time. This resulted in a noise level (the ratio of the variance due to random error and that due to real fluctuations) of smaller than 10%, judging from spatial correlations.

Uncorrelated vectors were occasionally observed in the PIV fields, despite the outlier detection applied in the Davis software. For the local statistics (Section 4), spurious data removal was applied as a post-processing step, outside of the PIV software. The conditioning of the PIV data on the boundary location strongly reduces scatter due to intermittency and generates data with a more symmetric distribution. After removing the unvalidated vectors from the data set, data points with a distance of more than three standard deviations from the median were removed. Generally, statistics (mean and variance) were only calculated for data sets of which less than 10% was removed (because of unvalidated vectors or outliers) to avoid statistical bias. The size of the data in the local coordinate system was in the order of several thousand values per point.

In principle, in a flow with temperature gradients, thermophoresis has an effect on small particles, such that the particle velocity is not equal to the flow velocity. This was elaborated on in Hasselbrink and Mungal [25], who concluded that in the presence of temperature gradients of 2000 K/mm, seeding particles such as used here can experience a differential velocity of 0.15 m/s. With a typical thickness of the flame zones in the order of a millimeter (from the OH-PLIF images), and the maximum instantaneous temperature rise of 400 K (from CARS measurements, [15]), the differential velocity due to thermophoresis is less than 0.05 m/s, and can be safely ignored.

To validate the results from the PIV system, the velocity field at a jet Reynolds number of 4100 has been compared with previous LDA data for this case [15]. Both the mean axial velocity field and the Reynolds stresses correspond very well with the earlier obtained LDA data: in the jet region, they are in agreement typically within 5–10%. The radial velocity in the coflow region is slightly more off (a difference of up to 25%), which is due to this velocity component being very small, at around 0.5 m/s.

2.4. OH-PLIF system and data processing

OH-PLIF images were taken simultaneously with the PIV recordings but at 10 Hz. Therefore, only one out of ten PIV fields could be used for conditional statistics. The OH-PLIF laser pulse was temporally centred between the two PIV pulses. The UV-light was generated by a Spectra Physics PRO250-10 Nd:YAG laser, pumping a Syrah PrecisionScan dye laser at 532 nm. The dye laser was operated with Rhodamine 590, generating light at 565.8 nm which was frequency-doubled to 282.9 nm, to excite the $Q_1(6)$ line of the $A^2\Sigma^+ - X^2\Pi(1,0)$ transition. The pulse energy at 282.9 nm was 10 mJ. The sheet was made 40 mm high with a thickness of 0.6 mm by the same optics as those of the PIV system, see Fig. 3. Overlapping of the PLIF sheet with the PIV sheet was done with a dichroic mirror. A Semrock narrow pass filter was used to block elastic scattering. Fluorescence was collected through a 105 mm Nikkor UV lens, and recorded by a Lambert Instruments HI-CAM CR camera, with a resulting imaging resolution of 85 μm per pixel. More details on the optical configuration of the PIV and OH-PLIF system are provided in [26]. A background image (with identical settings but no laser pulse) was subtracted from the images, and the pictures were smoothed with a Gaussian kernel with a FWHM of 8 pixels (~ 0.7 mm). Per case, 270 simultaneous OH-PLIF and PIV images are recorded for conditional statistics. The full PIV dataset is ten times larger, containing 2700 fields, which are used for unconditional statistics.

3. Conditional velocity statistics

3.1. OH-PLIF signal strength as flame indicator

In this paper, the OH fluorescence intensity is used to determine whether a region in space is chemically reactive or not. The OH

radical is not only present in regions with high reaction rates, as it survives relatively long in the post-flame region. Because the focus in this study is on the region where flame pockets are first formed, the OH radical will nevertheless provide a clear distinction between regions where no reaction has occurred yet and regions where conversion of the reactants takes place or has taken place. A quantitative measurement of the OH number density is not undertaken here. Conversion of the camera signal count into OH number densities requires careful consideration of, amongst others, laser light sheet intensity, temperature dependence of transitions, quenching effects, and the sensitivity of the imaging setup [27]. A recent study [28] shows that the latter is not trivial when an intensified high-speed camera is used. For instance, the time- and temperature dependent and non-linear response of the camera and intensifier should be dealt with.

For the limited purpose of flame detection the demands on the OH measurements are less strict. Spatial inhomogeneity of the laser light sheet was minimised in this study by making the light sheet approximately twice as high (in z-direction) as the region of interest. Thresholding was applied to distinguish the flame regions from non-flame regions. To investigate which threshold level might be appropriate, the distribution of OH signal counts was studied. Figure 4 shows the complementary cumulative density function CCDF, (which is defined as the probability that a value is exceeded) plotted logarithmically against the number of counts. It is linear over a large extent indicating an exponential distribution. A break in the slope is seen at a count level of roughly 15. The part below this value corresponds to the weak OH-PLIF signal in the hot coflow. The part above this value is related to the presence of flame zones. The conditional flow field, as presented later in this section, is thus derived from only those vectors that coincide (in time and space) with the presence of an OH-PLIF signal that exceeds the threshold value. An OH signal count of 30 was chosen as the default threshold value to distinguish reactive from non-reactive regions. This threshold results also in a satisfactory visual division between “flame” and “no-flame” zones. In fact, any threshold value between 25 and 40 can be chosen, with negligible impact on the conditional and local velocity and vorticity profiles. For convenience, regions with OH-levels exceeding the threshold value will be called “flame zones”, although the OH-rich regions do not necessarily cover the entire zone where reactions take place.

3.2. Visual and OH-PLIF observations

The seeding particles as used for the PIV measurements can be used to visualise the jet. Although these particles do not diffuse like gas molecules do, the particles and gases undergo the same turbulent mixing. By imaging of the Mie scattering of the seeding particles in a turbulent jet, one can capture the large scale mixing

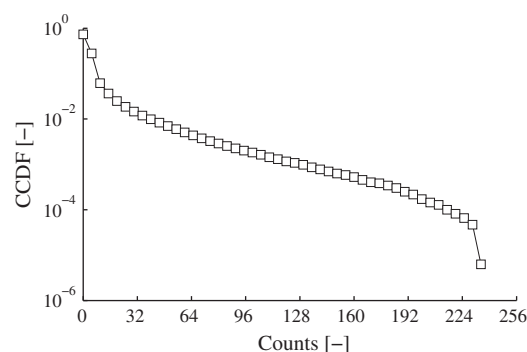


Fig. 4. The CCDF of the number of counts of the OH signal, for all OH statistics at $z = 70$ mm, case DNG 4.5.

features very well, leading to results that are roughly comparable to mixture fraction imaging with a fluorescent tracer molecule, see Long et al. [29]. A straightforward method of visualising the positioning of the flame zone relative to the mixing field is thus to strongly seed the jet and not seed the coflow, and do simultaneous OH-PLIF imaging and Mie scattering imaging (with an identical setup as used for the PIV recordings). The resulting superimposed simultaneous Mie scattering- and OH-PLIF images are shown in Fig. 5. Figure 6 shows such images in greater detail.

The spatial separation between the flame and the seeding regions is evident in both figures. Long et al. [29] also find that tracer molecules in their turbulent jet extend somewhat beyond the tracer particles. A straightforward explanation is that the tracer molecules are additionally transported by molecular diffusion. These images are thus an indication that the flame zone is located in a region beyond that where turbulent transport of the jet dominates.

3.3. Conditional and unconditional flow field

The mean axial and radial velocities, both unconditional and conditional, are compared in Fig. 7. The conditional statistics are plotted with error bars, that have a total length of two times the rms divided by the square root of the number of data points, to indicate the statistical uncertainty. The flame probability (the fraction of images that contains an identified flame at $z = 65$ mm as a function of r) is also shown in Fig. 7a. Note that the case DNG 4.5 suffers from some left–right asymmetry.

The axial velocity is somewhat smaller conditional on flame presence. In conventional flames, one might expect an influence of the flow divergence on the (axial) velocity due to the large decrease in density in the flame zone. In these flames, the relative temperature increase due to reactions is very moderate, and the velocity field is not noticeably affected by the flame [15]. A larger difference is seen in the radial velocities. Regions with strong OH signals move laterally inward faster than regions without, close to the centreline. This is due to the entrainment at the jet interface: ambient fluid is carried toward the jet, whereas the fluid that is part of the jet moves outward rather than inward, causing spreading of the jet. This strong correlation between radical species concentration and radial velocity is directly related to the turbulent scalar flux of the species concentration, and to that of the mixture fraction.

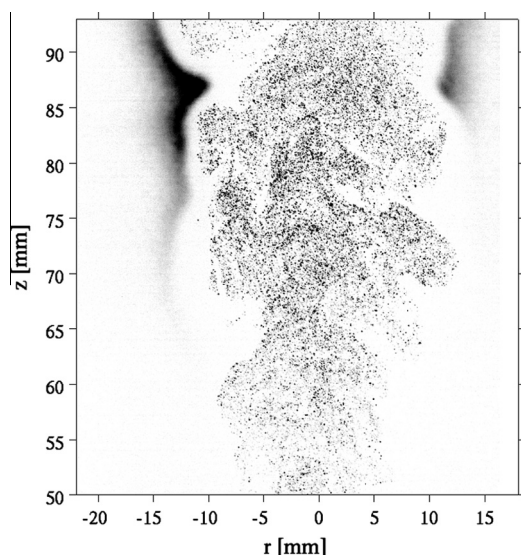


Fig. 5. The raw image from the PIV camera superimposed on the PLIF image, DNG 4.5 case ($Re_{jet} = 8800$). The PLIF sheet is somewhat higher for visualisation purposes.

The conditional and unconditional mean vorticity is shown in Fig. 8. A drastic difference is seen here. Conditional on flame presence, the magnitude of the vorticity remains close to the low values of the coflow, apparently unaffected by the jet.

The results for the conditional axial velocity, radial velocity and vorticity show that conditional on flame presence, these quantities assume values that are typical for the coflow. This finding connects well to the conclusion of the previous section. Furthermore, it means that the flow field at the mean flame location is intermittent: the flow alternates from being turbulent to being quasi-laminar, when a patch of irrotational coflow fluid passes by.

4. Local velocity field

In this section, the flow field in the neighbourhood of flame zones is investigated by introducing local coordinate systems attached to the instantaneous flame zones. The reason for this approach is that both the flame zones and the velocity field get transported by the same large turbulent structures. Therefore, by this positioning on the flame zone location, the “smearing” effect due to large scale turbulent motions is undone, and a sharper picture of the local velocity field emerges even when this velocity field is averaged. The orientation and the origin of the local coordinate systems are determined based on the OH-PLIF images, as elaborated in the following.

4.1. Methodology

In addition to occasionally appearing strong OH signals from flame zones, a certain minimum level of OH appears to be always present in the coflow. This is caused by the high coflow temperatures, such that the equilibrium concentrations are sufficiently large to be detected. Whereas this “background” OH signal is found throughout most of the coflow, it drops sharply to a near-zero value close to the jet/coflow interface. Apparently, the OH radicals in the coflow fluid are destroyed very quickly as this fluid is entrained, which is due to the chain terminating reactions occurring in fuel-rich regions [30]. This is confirmed by the disappearing of the sharp interface between the coflow and jet fluid when air is supplied through the central jet instead of methane or natural gas (not shown). The interface is therefore an indicator for the jet interface, separating low- and high mixture fraction regions. Due to its sharpness, it provides a convenient reference frame for the conditioning. The OH-PLIF data is thus used not only to identify the flame region, but also to identify the jet boundary. This is done with a much lower threshold level (11 counts) that was chosen based on visual inspection. The exact level of this threshold was more critical than that of the flame zones. Inspection of all images by eye showed that this threshold resulted in a correct tracing of the jet boundary. The resulting boundary is indicated by the dashed line, in the top figure of Fig. 9. The arrays of r - and z -coordinates that describe the interface are each smoothed using a rectangular window with a length of 11 pixels (~ 1.0 mm) to reduce the effects of the pixel quantisation. A material interface is detected in each image, both near to and far from regions with high OH-PLIF intensities.

A problem of using this interface directly for the conditioning is that the location of the interface is influenced by the presence of nearby strong OH signals due to blurring of the image intensifier and, to a lesser extent, by the image smoothing. This is confirmed by inspection of statistics conditional on the presence and the absence of flame zones at a height of 70 mm. The interface is seen to be located on average 1.5 mm more radially inward conditional on flame presence. Of the velocity field. Despite the disturbing effect of strong OH signals on the location of the perceived interface, the

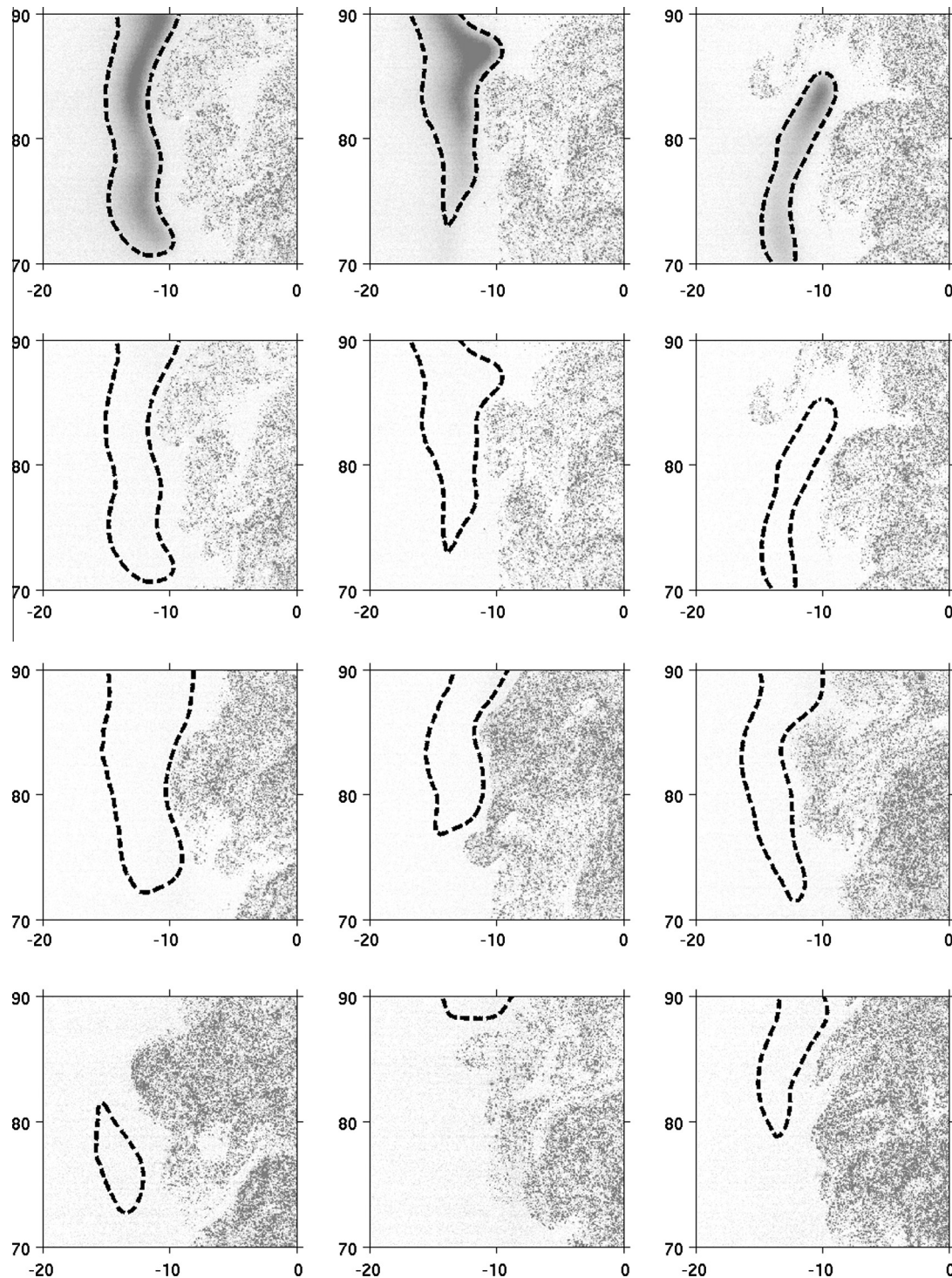


Fig. 6. Nine simultaneous OH-PLIF and seeding snapshots. The upper three figures have the OH-PLIF and seeding images superimposed, to illustrate how the threshold criterion functions to detect flame zones. Below, only the detected flame contours are shown, to make the distinction between the seeding and flame zones more clearly. The upper row and the second row from the top represent identical images. Note that the flame zones are folded closely to, but always outside, the seeded part of the jet.

orientation of the interface appears nevertheless to be well correlated with that of the OH contours. The direction of the normal to the interface is therefore used as a coordinate axis for the conditioning, its origin is however not based on the location of the interface, but on the OH profile along the normal.

This is done by first normalising the OH-PLIF values along the normal between zero and one. The origin is shifted such that the normalised intensity value of 0.5 is located at $s = 0$. The non-integer

shift is accomplished by performing interpolation along the profiles. This normalisation procedure is shown in Fig. 10. The regions of the flame zone closest to the jet (roughly from $s = -1$ mm to 1 mm) lie very close together, such that $s = 0$ forms a good measure for the fuel-rich edge of the flame-contour. The white dots in the bottom figure of Fig. 9 indicate $s = 0$ for the shown profiles. Finally, arrays of global coordinates are calculated (the dots in the lower two figures of Fig. 9) that correspond to points on an axis s , onto

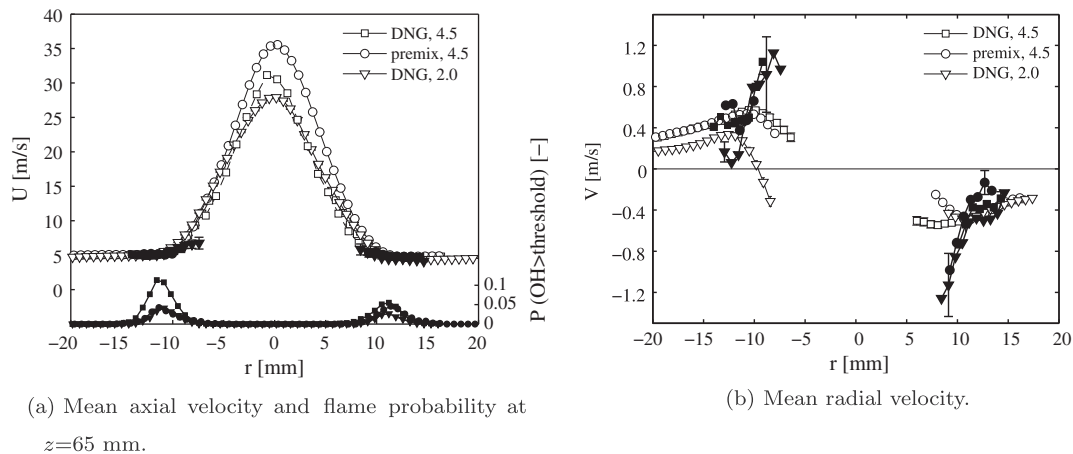


Fig. 7. Unconditional (open symbols) and conditional (solid symbols) axial and radial velocities, at $z = 65$ mm. The lower graphs in Fig. 7a correspond to the right axis and indicate the probability of flame presence at $z = 65$ mm. For the DNG 4.5 case, LDA measurements at $z = 60$ mm were added. To avoid cluttering, only a few error bars pertaining to the conditional data are plotted in Fig. 7b.

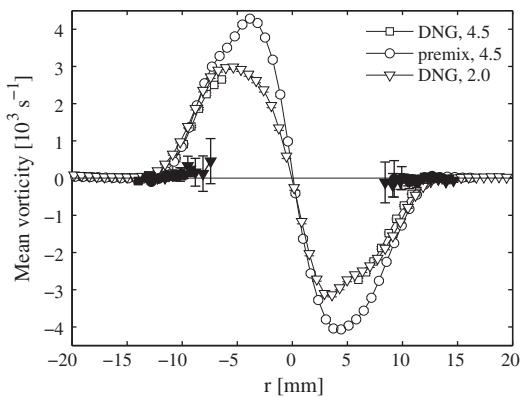


Fig. 8. The mean vorticity at $z = 65$ mm, unconditional (open symbols) and conditional (solid symbols).

which the OH and PIV values are interpolated linearly. Values of s increase from the oxidiser side toward the fuel side.

Note that the reported thicknesses and distances are *projected* thicknesses and distances. In measurements on non-reacting turbulent jets, actual (three-dimensional) thicknesses were shown to be on average around 20% smaller than the measured two-dimensional counterparts [31]. The real thickness of the OH-contours is thus expected to be smaller than the displayed thickness, not only due to the effect of smearing but also due to the fact that the sections through the OH-structures do not always follow the shortest path.

Summarising, a hybrid approach is used to generate local coordinate systems, combining the spatial information on both a low-level OH signal threshold (which can be interpreted as the material interface, albeit possibly shifted due to stronger OH signals) to give the orientation, and on a higher-level threshold, that determines the origin of these local coordinate systems. The benefit of this combination is that it avoids directional ambiguity (the perceived interface always runs from the bottom to the top of the image thereby separating the jet region from the coflow region, whereas the identified flame contours do not). Furthermore, the wrinkling of the flame contours is captured, providing a more realistic measure for the distance from the flame zone boundary.

4.2. Interface statistics

Statistics of the material interface can be obtained by only considering the interface, i.e., conditionally on the *absence* of a strong

OH signal, such that it is not disturbed by blurring of nearby strong signals. For the statistics to be valid for the (unconditional) jet-coflow interface, the presence of flame zones should be uncorrelated with the statistics of this interface. The absence of correlation cannot be verified, but the statistics briefly discussed in this section are all based on this assumption. The mean jet radii, as given earlier in Table 1, were determined by taking the conditional mean of the interface, at $z = 70$ mm. By determining mean radii at several heights, the spreading rate of the jet could be determined, which was in all cases close to 0.14. As a comparison, the value of the spreading rate of jets (based on scalar measurements) is approximately 0.11, for a wide range of density differences [32]. In these experiments, the jet half-width was however calculated as the point where the mean scalar concentration is half of that on the centreline.

An interesting characteristic of the interface is its wrinkledness, that is, the mean path length of the interface, compared to the length of the mean interface. This cannot be calculated by conventional methods (i.e., following the entire interface curve for each frame), because of the distorting effect of the strong OH signals in the flame zones. It can however be reconstructed from the conditional interface statistics, by looking at the scatter of the orientation vectors. Visually, this would be done by placing all interface orientation vectors of unit length head-to-tail, and dividing their cumulative length through the number of vectors. Mathematically, this can be written down succinctly using complex notation. The “alignment” of vectors is then given by

$$\alpha' = \text{abs}[\overline{\exp(i \alpha_{no})}], \quad (1)$$

where α_{no} indicates the surface angle that is determined conditional on the absence of strong OH signals along s . α' has value one when all vectors point in the identical direction, and is zero when the angles are distributed evenly. The sought-after wrinkledness now follows as the inverse of α' . If all vectors point in the same direction the wrinkledness is one (the interface is always the same straight line). If the interface is a sawtooth with perpendicular line sections of equal length, the wrinkledness equals the square root of two. The length along this sawtooth curve is thus square root of two times as long as a straight line from beginning to end.

The estimated wrinkledness in all studied flames is $1/\alpha' = 1.10$. This means that the length along the interface curve (following all wiggles) is on average 10% larger than the straight line connecting begin- and end points. In agreement with observations, the interface is thus not corrugated strongly. For a fractal structure,

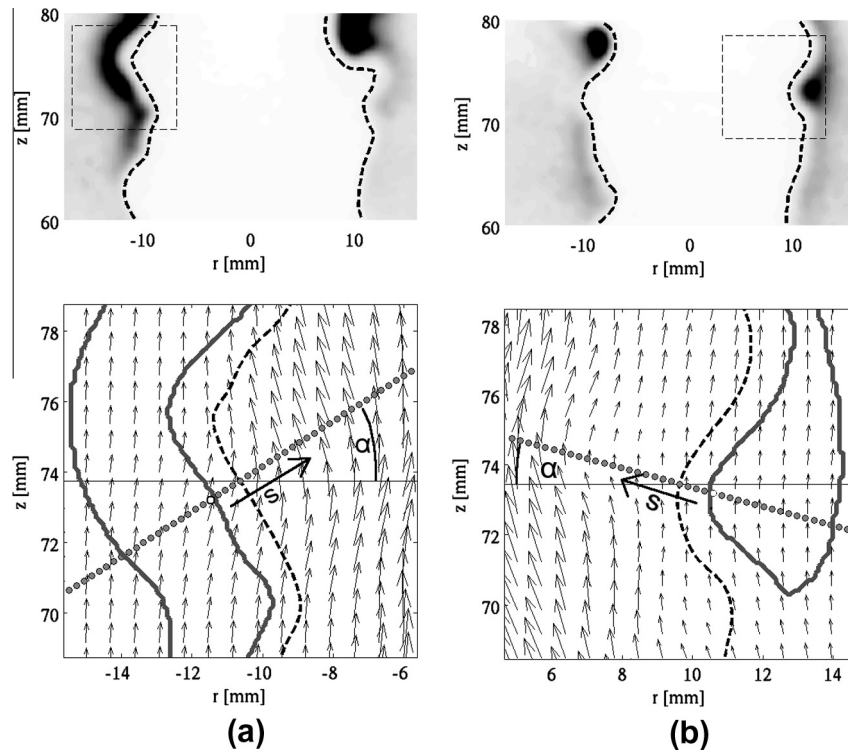


Fig. 9. Top two figures: instantaneous OH-PLIF images, with the jet boundary indicated by the dashed line. The region in the box is enlarged in the two lower figures, showing the velocity vectors, the jet boundary (dashed line) and the region which is recognised as a flame zone (grey thick line). The grey dots indicate the local coordinate s which is directed normal to the jet boundary, with 0.25 mm increments. This is the grid upon which the velocity field is interpolated to study the local velocity statistics (the local velocity field). The origin of s is indicated by the white dots, the positive direction of s runs towards the side of the jet. The positive direction of angles in this local coordinate system is indicated by the angle α .

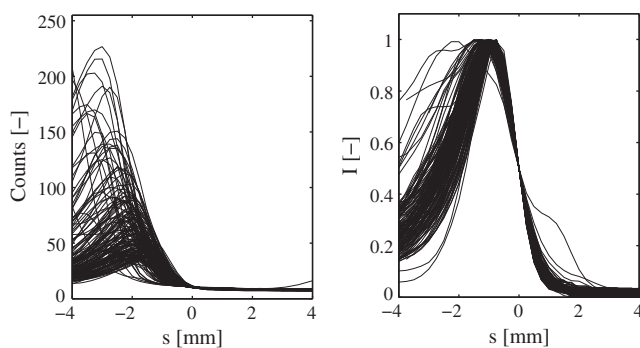


Fig. 10. The OH-PLIF profiles of 150 curves in the local coordinate s , before (left) and after (right) normalisation.

the total length is, up to a certain point, dependent on the level of detail with which the curve is observed. In this case, the smallest physical details appear to be in the order of one millimetre, i.e., further zooming in will not increase the wrinkledness.

4.3. Local velocities

The axial and radial velocities determine for a large part the mean transport of scalars. The axial velocity is of particular relevance to the downstream transport of newly formed flame pockets. The radial velocity determines the entrainment of coflow fluid, which brings hot oxidiser toward the fuel stream. These velocities, as a function of the distance from the normalised OH profile, are shown in Fig. 11. The axial velocity at the peak of the OH contour is hardly influenced by that of the jet. The radial velocity is seen to

be directed toward the centre line, and peaks at the fuel-rich side of the flame region ($s > 0$). This peak is not as high as that of the conditional mean radial velocity (Fig. 7). The radial velocity thus depends more strongly on the radial location of the flame zone, than on the relative location within the flame zone. The axial velocity is almost constant within the complete flame region, assuming the value of the coflow velocity. When normalised with the local jet centreline velocity, the coflow velocity and the mean jet radius, the profiles become very similar. It is seen that the profiles of the partially premixed flame lie somewhat closer to the flame. It is tempting to attribute this to the different stoichiometry of the fuel. The difference is however rather small (~ 0.5 mm).

4.4. Vorticity and enstrophy

Figure 12a shows the local vorticity field, as a function of the distance s . The vorticity is positive in the direction of positive angles in the local coordinate system (see α in Fig. 9), such that the counter-clockwise rotation for the global coordinate $r < 0$, and a clockwise rotation at $r > 0$ are both counted as positive. It is seen that in all three cases, the mean vorticity near the centre of the flame zones is identical to that further into the coflow, with a value very close to zero. When normalised with the local jet width and the centreline velocity, the profiles again become comparable, the premixed case being again somewhat closer towards the flame region. Note that the curve of the mean vorticity of case DNG 2.0 in Fig. 12b, is partially obscured by that of case DNG 4.5. Comparing with the global vorticity profiles (Fig. 8), the introduction of local coordinates successfully reduces the smearing effect of the large scale structures: the mean vorticity profile is around four times steeper when plotted in the local coordinate s as opposed to that plotted in the global coordinate r .

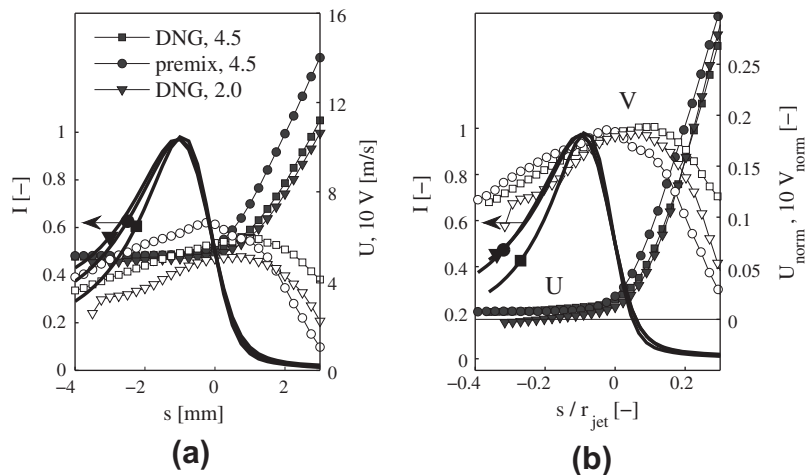


Fig. 11. The radial and axial velocities, for the three cases. The thick line indicates the mean normalised OH profile. The open symbols correspond to the radial velocity V the closed symbols correspond to the axial velocity U . In the figure at the right hand side, the velocities are normalised. The normalisation of V is $V_{\text{norm}} = V/U_{\text{jet}}$, U is normalised as $U_{\text{norm}} = (U - U_{\text{co}})(U_{\text{jet}} - U_{\text{co}})^{-1}$.

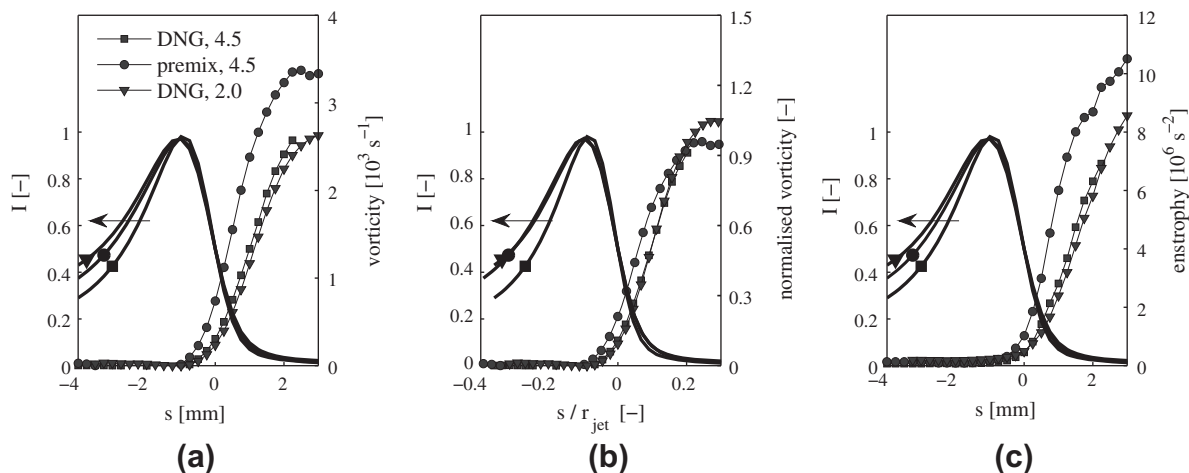


Fig. 12. The mean local vorticity (a), the normalised mean vorticity (b) and the enstrophy (c), along with the normalised mean OH signal. The vorticity was normalised with the local centreline jet velocity and the mean radial distance of the material interface: $\omega_{\text{norm}} = \omega r_{\text{jet}}/U_{\text{jet}}$.

The local enstrophy (here taken as the mean square of the vorticity fluctuations) is very small for $s < -0.5$ mm (typically $160 \times 10^3 \text{ s}^{-2}$ without smoothing and $60 \times 10^3 \text{ s}^{-2}$ with smoothing), whereas it increases strongly for $s > 0$ (to over $8 \times 10^6 \text{ s}^{-2}$ at $s = 3$ mm in all cases without smoothing, $6 \times 10^6 \text{ s}^{-2}$ with smoothing). Since the smallest scales of the turbulent flow are not resolved, the values in the turbulent jet can be considered to be lower estimates.

4.5. Strain rates

The local strain rate is a key quantity in chemistry-turbulence interaction. Strains that are compressive in the direction of the scalar gradients, act to augment these gradients. In the infinitely fast chemistry limit, the instantaneous reaction rate is proportional to the square of the mixture fraction gradient [33]. On the other hand, when the chemistry time scales are of the same order of magnitude as the diffusive time scales (commonly expressed as the inverse of the scalar dissipation rate), extinction might occur. Also, autoignition might be inhibited by large strains, as was first derived by means of an asymptotic analysis by Liñan and Williams [6]. Of interest to the studied flames is therefore the local strain rate,

i.e., the compression or extension of the flame surface. To facilitate the analysis of the local flow field, the symmetric part of the instantaneous velocity gradient tensor (the strain rate tensor) is diagonalised, such that instead of three strains in the laboratory coordinates (e_{xx} , e_{xy} and e_{yy}) two principal strains (ϵ_1 and ϵ_2) and the angle θ_1 of the largest principal strain are obtained. Next, the diagonalised strain tensor can be rotated in the direction of the normal of the interface over an angle $\phi = \alpha - \theta_1$ to obtain the value of the strain normal to the interface, e_{11} . The intermediate step (resulting in the principal strains and the direction of the most extensional strain) is useful, because of the clear physical interpretation of the difference between the two angles α and θ , as the alignment between the direction of flow deformation and the gradient of the scalar field.

As a first step of the analysis, the statistics of the principal strain angle are examined. When dealing with the statistics of the principal axes, standard methods of averaging will not work because of the circular periodicity. That is, the average of a set of angles is in general dependent on the choice of the reference angle. For instance, the average of the two angles 10° and 350° would be calculated as 180° instead of 0° . This problem can be solved by adding the vectors corresponding to the angles and calculating the angle

of the resulting vector. In this case the periodicity of the principal axis over 1π radians must also be taken into account. This is achieved by the following operations on the angle θ . First, the angular values are evaluated modulo π according to:

$$\tau = 2(\theta \bmod \pi), \quad (2)$$

after which the values of τ are averaged. The factor 2 is included in Eq. (2) to make principal axes that are orientated perpendicularly (have an angular difference of $\pi/2$) cancel out (relevant only for the calculation of τ' , Eq. (3)). Written as an averaging operation in the complex plane (as was done earlier in Eq. (1)), two quantities can be obtained:

$$\bar{\tau} = \arg[\exp(i \bar{\tau})] \quad \text{and} \quad \tau' = \text{abs}[\exp(i \bar{\tau})]. \quad (3)$$

The first term is the angle of the average vector in the complex plane. The second term is a measure for the alignment of the vectors; it takes a value of one when the direction of the axes are all the same, and a value of zero when this direction is distributed evenly in all directions. As a final step, $\bar{\theta}_1$ is calculated as $\bar{\tau}/2$. The statistics of θ and the principal strains are shown in Fig. 13, for three values of s . The largest extensional strain is on average directed obliquely into the jet (the principal direction θ_1 is within 10% of $\pi/4$), which is a pure shear deformation in the original (r, z) coordinate system. The variation is relatively small, especially for $s > 0$ (the value of τ' in Eq. (3) equals 0.8 at $s = 2$). The larger scatter in θ_1 for $s < 0$ is attributed to a larger relative error in the PIV measurements. The deformation of the flame interface is thus mainly a shearing deformation.

The variation of the principal angle and principal strains for the three cases, as a function of s is displayed in Fig. 14. Note that the strain curves of DNG 4.5 and DNG 2.0 lie on top of each other in the left figure, obscuring the results of case DNG 4.5.

For the flame zone, naturally, the local statistics of the stretch or compression are relevant. Rotation of the principal strain tensor from the principal angle to the normal of the interface α will yield the local normal strain:

$$e_{11} = \epsilon_1 \cos^2(\phi) + \epsilon_2 \sin^2(\phi) \approx \frac{1}{2}(\bar{\epsilon}_2 + \bar{\epsilon}_1) \quad (4)$$

where ϕ is the difference between θ_1 and α , because θ_1 is approximately $\pi/4$ and α has a value close to zero. Because of the small fluctuations in the angles, the average value of the local normal strain can be approximated by: $\bar{e}_{11} \approx 0.5(\bar{\epsilon}_2 + \bar{\epsilon}_1)$. For axisymmetric, incompressible problems, continuity requires that the sum of the normal stresses plus the term V/r is zero (see for instance [34],

pg. 78). The latter term is found to be an order of magnitude smaller than the normal stresses. Ignoring the relatively small density differences in the continuity equation, it follows that the absolute value of e_{11} is much smaller than the absolute values of e_1 and e_2 . The mean normal strain is thus very small compared to the principal strains and this is confirmed by the thin lines in Fig. 14. Only for larger values of s , does the normal strain on average become compressive. The maximum average compressive stress is 380 s^{-1} at $s = 1.5 \text{ mm}$, for the case premix 4.5. The mean deformation in the direction of the interface at $s < 0$ is thus neither strongly (compared to the magnitude of the normal stresses) compressive nor extensional. The normalised correlation between α and θ peaks in all cases at $s = 2.75 \text{ mm}$, and is rather moderate, between 0.16 (case DNG, 2.0 mm) and 0.23 (premixed case). The probability distribution of the normal strain is rather symmetric around zero normal strain, and becomes much wider for larger values of s . The pdf's of the strain normal to the flame surface, at three different values of s , are shown in Fig. 15. Comparing with Fig. 13, the stronger extremes in principal strain are due to an increase in normal strains, whereas the scatter in principal angle actually decreases. At $s = 0$, the 10th percentile of the compressive strain lies between $-1 \times 10^3 \text{ s}^{-1}$ (case DNG 4.5) and $-1.5 \times 10^3 \text{ s}^{-1}$ (case premixed 4.5).

To investigate the influence of spatial resolution, the normal strains were also computed for the smoothed PIV fields, and compared with the presented, non-smoothed results. The ratio of the rms of normal strain determined with the non-smoothed and smoothed data has a minimum at $s = 0$, with a value of 1.2. There are two reasons that smoothing reduces variance in strain fields. Firstly, noise resulting from the random error is reduced and secondly, strains occurring on smaller length scales are filtered out. Taking into account the sharp division of the flow field left and right from $s = 0$, it is expected that the rms of the normal strain of the non-smoothed data are somewhat overestimated for $s < 0$ due to noise (the smoothed fields result in a 35% lower mean value of ϵ_{11} at $s = -1$). In the direction toward the jet, it is likely underestimated, as the limited spatial resolution leads to a cut-off of the dissipation spectrum. At $s = 2$, smoothing results in a reduction in the mean value of ϵ_{11} of 25%.

5. Evaluation and discussion of the results

In Section 3, the presence of flame structures in the quasi-laminar part of the flow was made apparent visually and by comparing conditional and non-conditional velocity statistics. In particular, it

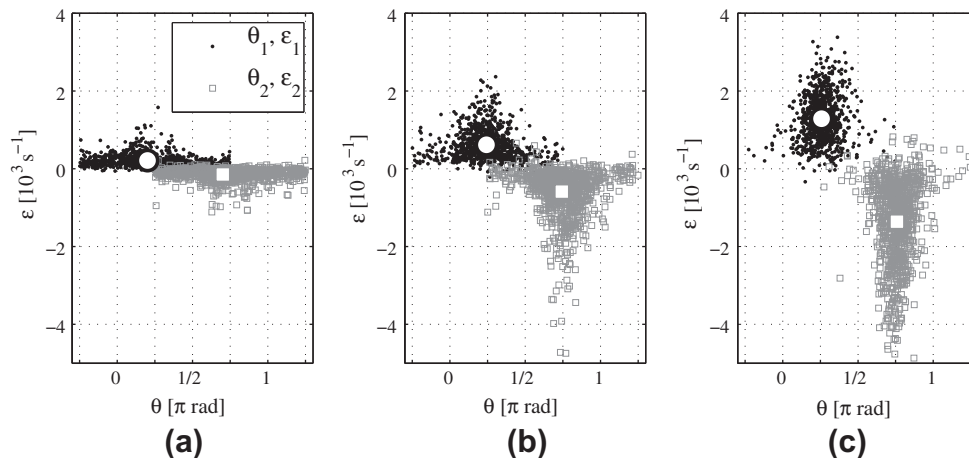


Fig. 13. Scatter plot of θ_1 with ϵ_1 and θ_2 with ϵ_2 , at $s = -3 \text{ mm}$, 0 mm and 2 mm . The large markers indicate the mean values. θ_1 is plotted modulo π , centred around $\pi/4$. Values of θ_2 (the angle of the most compressive direction) are, by definition, shifted by $\pi/2$ with respect to θ_1 . Case DNG 4.5.

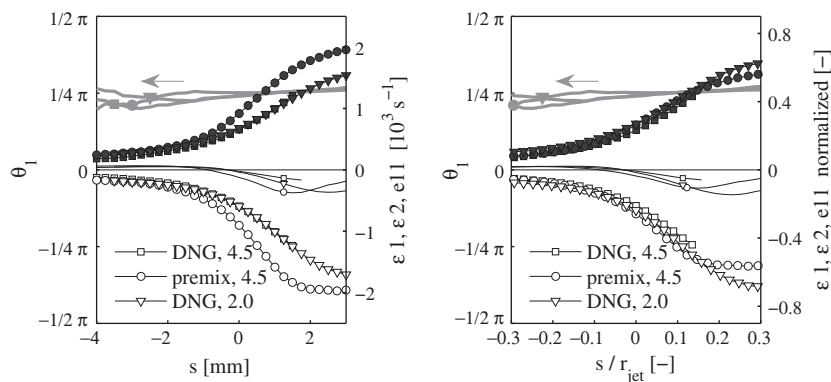


Fig. 14. The mean of the principal angle θ_1 (solid grey line, left axis) and the mean value of the principle strains ϵ_1 (closed symbols) and ϵ_2 (open symbols). The mean local normal strain is indicated by the thin lines. In the right figure, the distance is normalised, and the strains are normalised by $\epsilon_{\text{norm}} = \epsilon r_{\text{jet}}/U_{\text{jet}}$.

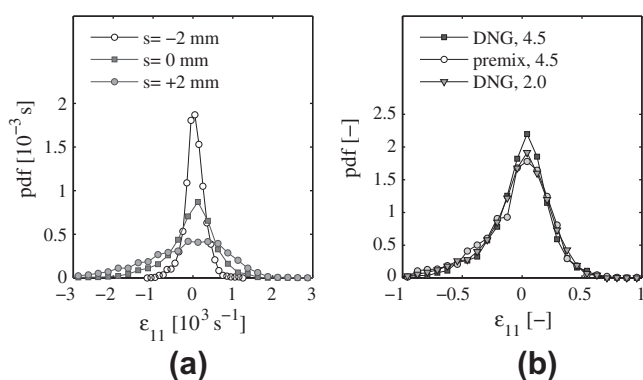


Fig. 15. Pdfs of the value of the strain normal to the flame contour (negative strain is compressive), at three locations, case DNG 4.5 (a), and pdfs of the normalised normal strain at $s = 0$, three cases (b). The strain is again normalised by $\epsilon_{\text{norm}} = \epsilon r_{\text{jet}}/U_{\text{jet}}$.

was shown that the flame resides outside of the region were seeding particles are mixed by the turbulence, that vorticity and axial velocity in the flame zones assume values typical for the coflow, and that the flame zones move radially inward toward the jet, i.e., are being entrained rather than have been entrained already. In Sections 4.3 and 4.4, velocity statistics were explored in a local coordinate system with distances relative to the OH signal profile. Plots of the vorticity and its variance (the enstrophy) showed that the separation between the quasi-laminar flow and turbulent flow is sharp. For $s < 0$, these quantities are very small compared to those a mere one millimetre (around a tenth of the mean jet radius) further into the jet region.

The fuel-rich side of the OH contours ($s \sim 0.5$ mm) therefore coincides with a boundary that sharply divides the instantaneous flow field between a turbulent, jet-influenced region and a quasi-laminar, coflow-influenced region. The existence of a sharp boundary layer, called the viscous superlayer, that separates a turbulent core flow from the irrotational surrounding flow is a well known phenomenon in turbulent shear flows [35,36] (pg. 138), [37] (pg. 167 and further).

In Section 4.5, the direction of the principle strains, and their alignment with the flame interface was examined. The principal strain axis was found to be at an angle of $\pi/4$ radians, or 45 degrees, with a direction radially inward and axially upward. The flame is alternatively compressed and stretched with roughly equal magnitude and probability. At the fuel-rich edge of the flame zones ($s = 0$), compressive strains exceeding $0.5 U_{\text{jet}} r_{\text{jet}}^{-1}$ (about 1300 s^{-1} in the DNG 4.5 case) are rare, with probabilities below 10%. The magnitude of the strains does not change nearly as strong

as that of the vorticity and its variance across the boundary. This can be understood from the transport equation of vorticity for constant density flows. Vorticity can diffuse and be intensified by vortex stretching, but not be produced by pressure fluctuations, unlike momentum. Indeed, it is well known that the material interface of a gaseous jet (i.e., a jet with a Schmidt number somewhat below unity) lies outside of the shear layer [38]. The “material interface” in the current context refers to the interface that separates fluid that contains material from the jet (i.e., mixture fraction greater than some very small value) from the fluid that does not.

Although the term “flame zones” was used to indicate regions with strong OH signals, the OH radical does not cover the entire flame zone. Fuel decomposition reactions take place in more fuel-rich regions, where for instance the CH radical is found. Despite the gap between the OH and the CH radical being small (Donbar et al. [39] mention a gap size of 0.5 mm in a conventional non-premixed flame of methane/nitrogen), a strong difference between velocity statistics conditional on OH and CH contours has been reported on the same setup. For instance, at $z/D \approx 17.5$, the vorticity at the OH contours was on average near zero, whereas the mean vorticity at the CH contours was $1.2 U_{\text{jet}}/\delta$ [40]. Here, δ is the full jet width at half the centreline velocity, which is roughly comparable to r_{jet} used here. Also, the CH zones were not aligned with the compressive strain axes at that height, this did however occur at higher locations.

Another region of the flame, possibly not covered by the OH regions, is that where first autoignition reactions occur. In many studies, and in the calculations presented in the appendix, this is observed to be at very lean mixture fractions when the oxidiser is heated [2,5,8,41]. Though this might be true for laminar or two-dimensional calculations, it is not clear whether this is always the case in a three-dimensional situation. For instance, the experiments of Gordon et al. [12] show early stages of ignition (i.e., presence of formaldehyde without OH) relatively close to the centreline. Based on their 3D-DNS calculations of a H_2 flame in a heated coflow, Yoo et al. [5] conclude that autoignition nominally occurs on the fuel-lean side but occasionally originates from fuel-rich pockets. Whether the autoignition process in these flames is affected by turbulent small-scale strains or only by the large-scale deformations in the quasi-laminar region, is therefore debatable.

Considering the similarity between enstrophy and dissipation of turbulent kinetic energy [36], the region where high levels of OH are found, is not the region where turbulent kinetic energy is dissipated, and hence this region is not expected to be governed directly by the local value of the rate of dissipation of turbulent kinetic energy. Furthermore, the concept of local well-stirredness is not justified: a most characteristic feature is the strong intermittency between the turbulent jet region and the irrotational coflow.

Employing a turbulent timescale to provide a closure for the mean reaction rate based on mean quantities [42,43] therefore seems to be an invalid approach for these flames.

Despite variations in fuel composition and nozzle diameter, the results for all cases were very similar after normalisation. This indicates the robustness of the results: the emerging picture is not limited to the near-field of the jet, nor to fuel/coflow combinations with a very low stoichiometric mixture fraction. Thus, also the higher stoichiometric mixture fraction contour of case “premix 4.5” appears to lie outside of the viscous superlayer (the sharp interface separating the turbulent from the non-turbulent flow), although Fig. 12 does seem to suggest a slight shift of the reaction zone toward the turbulent jet region for this case.

The correlation between low vorticity/strain and the presence of strong OH signals could be misinterpreted (especially in point measurements without simultaneous mixture fraction information) as a preference of the flame for such flow conditions, but this would imply an incorrect causality for these flames. Based on all discussed observations, the explanation is the positioning of the low mixture fraction fluid within the quasi-laminar coflow (i.e., outside the viscous superlayer), combined with the decisive role of the mixture fraction on chemistry (i.e., autoignition and reaction occurring at relatively low mixture fractions). This picture can be supported with fluid dynamics theory. Transport of mass and vorticity are both diffusive processes, which leads to a strong similarity between the viscous superlayer and the material interface of a turbulent jet. In gaseous jets, that have a Schmidt number somewhat smaller than one, the material interface is known to lie outside the viscous superlayer. Finally, it should be noted that in these flames, combustion does not significantly alter the flow field as is the case in conventional flames, because the volumetric expansion due to the flame is more than an order of magnitude smaller as that in conventional flames (concluded from earlier temperature measurements, [15]) [15].

6. Conclusions

Detailed conditional (i.e., conditional on the presence of flame zones) and local (i.e., considered in locally introduced coordinate systems relative to the flame zones) velocity data obtained with simultaneous PIV and OH-PLIF measurements were shown, for three different flames in the Delft jet-in-hot-coflow burner. These flames differed in jet diameter (and thereby in normalised axial distance) and level of premixedness (and thereby in stoichiometry). Despite these differences, the results were qualitatively similar, and almost identical after normalisation. The main results for the three flames can therefore be discussed as one single case.

The velocity data conditional on flame presence differed strongest from the unconditional data for the radial velocity and the mean and variance of vorticity. The conditional radial velocities are directed more strongly inward, indicating that the flame zones are part of the fluid that is entrained at the jet edge. The values of the conditional mean and variance of vorticity were orders of magnitude smaller than those in the shear layer of the jet. The local velocity data shows a very steep increase in the mean vorticity and its variance, a mere millimetre from what was defined to be the flame edge. These observations all show that the lean mixture fractions at which (most of the) chemical reactions take place lie just outside the viscous superlayer, the interface that separates the turbulent and non-turbulent part of the flow.

If the physics of these flame structures is to be captured within a RANS framework, a model is needed with a sound statistical basis. Specifically, it needs to deal with the fact that despite being on average in a high-shear, high-turbulence part of flow, the flames do not experience this turbulence.

The emerging picture of the flame structure is in contrast with industrial flameless burners, where the delaying effect of strong turbulent strains on ignition is considered to be the key to let mixing occur before combustion. It therefore appears that conclusions on turbulence-chemistry interaction drawn from these and similar laboratory flames cannot be generally projected onto industrial-sized flameless combustion burners, at least not without a careful analysis.

Appendix A. Autoignition delay time calculations

Autoignition delay time calculations were done with the program SENKIN [21], for the two fuels used (pure Dutch natural gas (DNG) and a mixture of air/DNG, 3:1 volumetric ratio). These autoignition calculations are zero-dimensional, progressing the chemical reactions from a single starting composition in time. Since it is not known beforehand at which mixture fraction autoignition occurs first, an array of mixture fractions was calculated for both fuels. This method is one of the proposed ways to compute the most reactive mixture fractions in [8], besides more involved 1-D calculations. The starting composition for each mixture fraction was obtained by the equilibrium chemistry program FLAME, with reactions turned off. The starting composition and temperature thus correspond to linear interpolation of the composition

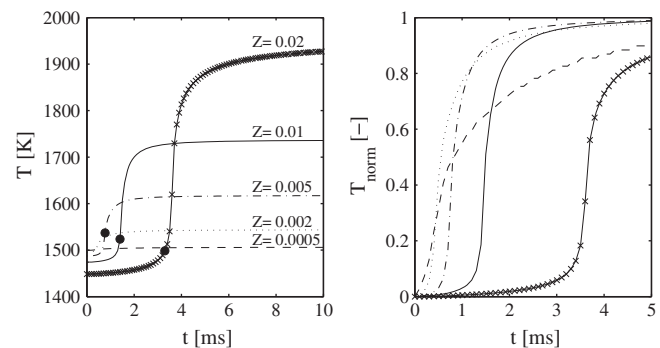


Fig. 16. Left figure: the transient temperature during autoignition for mixtures of DNG with hot coflow as an oxidiser, for several mixture fractions. The dots show the instant when the temperature increase exceeds 50 K, the used criterion for autoignition. The right figure has the temperature rescaled between its starting and end value (equilibrium temperature).

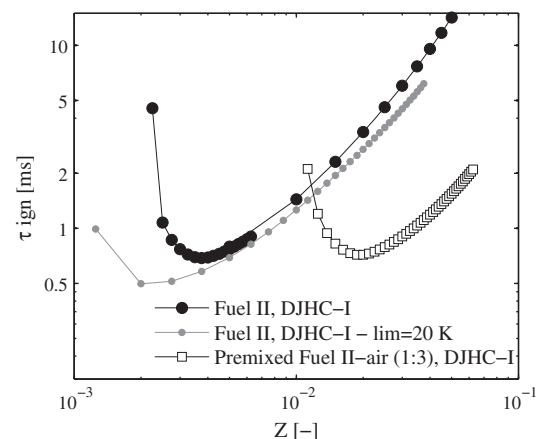


Fig. 17. Autoignition times for DNG and DNG premixed with air (1:3, volumetric ratio), for a range of mixture fractions. The oxidiser stream properties are $T_{co} = 1500$ K and $X_{O_2:co} = 5.5\%$ ($Y_{O_2:co} = 6.3\%$). The grey line illustrates the effect of lowering the autoignition temperature threshold from 50 K to 20 K.

and of the sensible enthalpy of the coflow and the fuel in mixture fraction space. The fuel composition and temperature (properties at mixture fraction one) are given in Section 2.2. The used oxidiser composition and temperature corresponds to that which is being entrained into the jet at $z = 60$ mm, which originates from $(z, r) = (3, 16)$ mm. This corresponds to a mass fraction of O_2 of 6.3% (mole fraction of 5.5%) and a temperature of 1500 K. An example of the autoignition process for several mixture fractions is given in Fig. 16. The left figure shows the temperature during autoignition, the right figure has the temperatures rescaled between their initial and end (the adiabatic flame temperature) values. To extract the most reactive mixture from the data, an autoignition time has to be defined for each simulated mixture fraction. Intuitively, the time at which the rate of change of temperature is highest would seem an appropriate choice. The problem encountered here is that this results in a most reactive mixture fraction that is so small, that the accompanying temperature increase (for instance, 10 K at the extremely lean mixture fraction of 0.0005) is so tiny it is most likely irrelevant. The second option is to introduce an arbitrary temperature threshold. This temperature threshold will directly influence the leanest mixture fraction that can be a candidate to be “most reactive” (as the maximum possible temperature decreases with decreasing mixture fraction). On the other hand, on the rich side the exact choice introduces little arbitrariness. To avoid unrealistically low mixture fractions as being most the reactive, the second option of thresholding is therefore applied here. The resulting autoignition delay times with a threshold of 50 K are shown in Fig. 17. It is seen that the choice for a lower threshold temperature affects the lean part of the graph, but not the rich part.

Despite the limitations imposed by the arbitrary choice of the temperature threshold, it can still be concluded that the ignition delay time is in the order of a millisecond for both pure and premixed DNG. Furthermore, the premixing shifts the range of mixture fractions where autoignition occurs first to the rich side. Interestingly, this shift follows the trend of the increase in stoichiometric mixture fraction due to premixing. This is possibly related to the smaller amount of CH_4 that is present in the premixed fuel, as CH_4 is known to have an inhibiting effect on chain branching reactions [30]. A value for the most reactive mixture fraction cannot be given based on these calculations. For this purpose, more elaborate 1-D calculations would be needed.

References

- [1] R.L. Gordon, A.R. Masri, S.B. Pope, G.M. Goldin, A numerical study of autoignition in turbulent lifted flames issuing into a vitiated co-flow, *Combust. Theor. Model.* 11 (3) (2007) 351–376.
- [2] R. Cabra, J.Y. Chen, R.W. Dibble, A.N. Karpetis, R.S. Barlow, Lifted methane-air jet flames in a vitiated coflow, *Combust. Flame* 143 (4) (2005) 491–506.
- [3] C.N. Markides, E. Mastorakos, An experimental study of hydrogen autoignition in a turbulent co-flow of heated air, *Proc. Combust. Inst.* 30 (2005) 883–891.
- [4] E. Oldenhof, M.J. Tummers, E.H. van Veen, D.J.E.M. Roekaerts, Ignition kernel formation and lift-off behaviour of jet-in-hot-coflow flames, *Combust. Flame* 157 (6) (2010) 1167–1178.
- [5] C.S. Yoo, R. Sankaran, J.H. Chen, Three-dimensional direct numerical simulation of a turbulent lifted hydrogen jet flame in heated coflow: flame stabilization and structure, *J. Fluid Mech.* 640 (2009) 453–481.
- [6] A. Liñán, F.A. Williams, Ignition in an unsteady mixing layer subject to strain and variable-pressure, *Combust. Flame* 95 (1–2) (1993) 31–46.
- [7] E. Mastorakos, T.A. Baritaud, T.J. Poinsot, Numerical simulations of autoignition in turbulent mixing flows, *Combust. Flame* 109 (1–2) (1997) 198–223.
- [8] E. Mastorakos, Ignition of turbulent non-premixed flames, *Prog. Energy Combust. Sci.* 35 (1) (2009) 57–97.
- [9] D. Tabacco, C. Innarella, C. Bruno, Theoretical and numerical investigation on flameless combustion, *Combust. Sci. Technol.* 174 (7) (2002) 1–35.
- [10] A. Cavaliere, M. de Joannon, Mild combustion, *Prog. Energy Combust. Sci.* 30 (4) (2004) 329–366.
- [11] B.B. Dally, A.N. Karpetis, R.S. Barlow, Structure of turbulent non-premixed jet flames in a diluted hot coflow, *Proc. Combust. Inst.* 29 (2002) 1147–1154.
- [12] R.L. Gordon, A.R. Masri, E. Mastorakos, Simultaneous Rayleigh temperature, OH- and CH_2O -LIF imaging of methane jets in a vitiated coflow, *Combust. Flame* 155 (2008) 95–181.
- [13] P.R. Medwell, P.A.M. Kalt, B.B. Dally, Simultaneous imaging of OH, formaldehyde, and temperature of turbulent non-premixed jet flames in a heated and diluted coflow, *Combust. Flame* 148 (1–2) (2007) 48–61.
- [14] Z.J. Wu, A.R. Masri, R.W. Bilger, An experimental investigation of the turbulence structure of a lifted H₂/N₂ jet flame in a vitiated co-flow, *Flow Turbul. Combust.* 76 (1) (2006) 61–81.
- [15] E. Oldenhof, M.J. Tummers, E.H. van Veen, D.J.E.M. Roekaerts, Role of entrainment in the stabilisation of jet-in-hot-coflow flames, *Combust. Flame* 158 (8) (2011) 1553–1563.
- [16] J.H. Frank, P.A.M. Kalt, R.W. Bilger, Measurements of conditional velocities in turbulent premixed flames by simultaneous OH-PLIF and PTV, *Combust. Flame* 116 (1–2) (1999) 220–232.
- [17] K.A. Watson, K.M. Lyons, J.M. Donbar, C.D. Carter, Scalar and velocity field measurements in a lifted CH_4 -air diffusion flame, *Combust. Flame* 117 (1–2) (1999) 257–271.
- [18] B. Böhm, C. Heeger, I. Boxx, W. Meier, A. Dreizler, Time-resolved conditional flow field statistics in extinguishing turbulent opposed jet flames using simultaneous highspeed PIV/OH-PLIF, *Proc. Combust. Inst.* 32 (2009) 1647–1654.
- [19] I. Boxx, C. Heeger, R. Gordon, B. Böhm, M. Aigner, A. Dreizler, W. Meier, Simultaneous three-component PIV/OH-PLIF measurements of a turbulent lifted, C₃H₈-argon jet diffusion flame at 1.5 kHz repetition rate, *Proc. Combust. Inst.* 32 (2009) 905–912.
- [20] K.R. Sreenivasan, On the scaling of the turbulence energy-dissipation rate, *Phys. Fluids* 27 (5) (1984) 1048–1051.
- [21] A. Lutz, R. Kee, J. Miller, Senkin: A Fortran Program for Predicting Homogeneous Gas Phase Chemical Kinetics with Sensitivity Analysis, Report No. SAND87-8248. UC-4. Technical Report, Sandia National Laboratories, 1987.
- [22] G.P. Smith, D.M. Golden, M. Frenklach, N.W. Moriarty, B. Eiteneer, M. Goldenberg, C.T. Bowman, R.K. Hanson, S. Song, W.C. Gardiner, V. Lissianski, Z. Qin, <http://www.me.berkeley.edu/gri_mech/>.
- [23] P. Lavoie, G. Avallone, F. Gregorio, G. Romano, R. Antonia, Spatial resolution of piv for the measurement of turbulence, *Exp. Fluids* 43 (1) (2007) 39–51.
- [24] M. Raffel, C. Willert, S. Wereley, J. Kompenhans, Particle Image Velocimetry, Springer-Verlag GmbH, 2007.
- [25] E.F. Hasselbrink, M.G. Mungal, Transverse jets and jet flames. Part 2. Velocity and OH field imaging, *J. Fluid Mech.* 443 (2001) 27–68.
- [26] E. Oldenhof, M.J. Tummers, E.H. van Veen, D.J.E.M. Roekaerts, Transient response of the Delft jet-in-hot coflow flames, *Combust. Flame* 159 (2) (2012) 697–706.
- [27] J.W. Daily, Laser induced fluorescence spectroscopy in flames, *Prog. Energy Combust. Sci.* 23 (2) (1997) 133–199.
- [28] V. Weber, J. Brübach, R.L. Gordon, A. Dreizler, Pixel-based characterisation of CMOS high-speed camera systems, *Appl. Phys. B Laser Optic.* 103 (2011) 421–433.
- [29] Marshall B. Long, Sten H. Staerner, Robert W. Bilger, Differential diffusion in jets using joint plif and lorenz-mie imaging, *Combust. Sci. Technology* 92 (4–6) (1993) 209–224.
- [30] R.W. Bilger, Reaction-rates in diffusion flames, *Combust. Flame* 30 (3) (1977) 277–284.
- [31] K.A. Buch, W.J.A. Dahm, Experimental study of the fine-scale structure of conserved scalar mixing in turbulent shear flows. Part 2., *J. Fluid Mech.* 364 (1998) 1–29.
- [32] C.D. Richards, W.M. Pitts, Global density effects on the self-preservation behavior of turbulent free jets, *J. Fluid Mech.* 254 (1993) 417–435.
- [33] R.W. Bilger, Structure of diffusion flames, *Combust. Sci. Technol.* 13 (1–6) (1976) 155–170.
- [34] G.K. Batchelor, An Introduction to Fluid Dynamics, Cambridge University Press, 2000.
- [35] S. Corrsin, A.L. Kistler, The Free-Stream Boundaries of Turbulent Flows. Technical Report, NACA Report 1244, 1955.
- [36] P.A. Davidson, Turbulence: An Introduction for Scientists and Engineers, Oxford University Press, 2004.
- [37] S.B. Pope, Turbulent Flows, Cambridge University Press, 2000.
- [38] R.W. Bilger, Turbulent-diffusion flames, *Annu. Rev. Fluid Mech.* 21 (1989) 101–135.
- [39] J.M. Donbar, J.F. Driscoll, C.D. Carter, Reaction zone structure in turbulent nonpremixed jet flames - from CH-OH-PLIF images, *Combust. Flame* 122 (1–2) (2000) 1–19.
- [40] P.S. Kothnur, M.S. Tsurikov, N.T. Clemens, J.M. Donbar, C.D. Carter, Planar imaging of CH, OH, and velocity in turbulent non-premixed jet flames, *Proc. Combust. Inst.* 29 (2) (2002) 1921–1927.
- [41] R.L. Gordon, A.R. Masri, E. Mastorakos, Heat release rate as represented by $[OH] \times [CH_2O]$ and its role in autoignition, *Combust. Theor. Model.* 13 (4) (2009) 645–670.
- [42] B.F. Magnussen, B.H. Hjertager, On mathematical modeling of turbulent combustion with special emphasis on soot formation and combustion, *Proc. Combust. Inst.* 16 (1) (1977) 719–729.
- [43] I.S. Ertesvag, B.F. Magnussen, The eddy dissipation turbulence energy cascade model, *Combust. Sci. Technol.* 159 (2000) 213–235.